Supporting information

Fast Photocatalytic Hydrogen Peroxide Generation by Singlet Oxygen-Engaged Sequential Excitation Energy and Electron Transfer Process

*Xiangkang Zeng [a, *], Tianyi Wang [b], Zhuyuan Wang [a], Mike Tebyetekerwa [a], Yue Liu [c], Zhuoyue Liu [d], Gen Wang [d], Ary Anggara Wibowo [e], Gregory Pierens [f], Qinfen Gu [g, *], and Xiwang Zhang [a, c*]*

[a] Dow Centre for Sustainable Engineering Innovation, School of Chemical Engineering, The University of Queensland, St Lucia, Queensland, 4072, Australia

[b] Advanced Institute for Materials Research (WPI-AIMR), Tohoku University, Sendai 980-8577, Japan

[c] Department of Chemical and Biological Engineering, Monash University, Clayton, VIC, 3800, Australia

[d] Shaanxi Key Laboratory of Environmental Engineering, School of Environmental and Municipal Engineering, Xi'an University of Architecture and Technology, Xi'an, Shaanxi 710055, PR China

[e] School of Engineering, The Australian National University, Canberra, Australian Capital Territory, 2601 Australia

[f] Centre for Advanced Imaging, The University of Queensland, St Lucia, Queensland, 4072, Australia

[g] Australian Synchrotron, ANSTO, 800 Blackburn Rd, Clayton, VIC, 3168, Australia

* Corresponding authors. Email: x.zeng@uq.edu.au (X. Zeng); qinfeng@ansto.gov.au (Q. Gu); xiwang.zhang@uq.edu.au (X. Zhang)

This Supplemental Information file includes:

Supplementary Text

Figures S1 to S36

Tables S1 to S4

References

Supplementary Text

FTIR (Figure S2)

The peak and binding energy (74.98 eV) of Al 2p in Al-TCPP are in line with that of aluminum oxyhydroxide (Al-OOH) [1], indicating the Al is connected with oxygen and hydroxyl groups. Besides, in the FTIR spectra (e and f), the broad peaks at 2978, 2655, and 2531 cm^{-1} corresponding to -OH stretch of carboxylic acid dispersed, while a new peak at 618 cm^{-1} corresponding to the Al-O group of aluminum oxyhydroxide[2] is present. These results collectively prove that Al^{3+} is coordinated with the carboxylate-derived oxygen atoms of TCPP and two μ_2 axial-OH groups to form infinite $Al(OH)O_4$ chain in Al-TCPP[3]

BET surface area (Figure S6).

N_2 adsorption and desorption of Al-TCPP was performed on one 3Flex (Micromeritics) instrument at 77K. At this temperature, the diffusion of N_2 to micropore is very slow, and the slow diffusional limitations at this temperature might influence adsorption in carbon ultramicropores (pores smaller than 7 Å)[4]. Due to this reason, the ultramicropores (smaller than 7 Å) are not detected via N_2 adsorption at 77K. To further reveal the porosity of Al-TCPP, we performed the analysis with a TriStar (Micromeritics) by CO_2 adsorption at 273K. CO_2 molecules at 273K can more easily access ultramicropores than N_2 at 77 K even though the critical molecular dimensions of both gases are similar [4]. According to the density functional theory (DFT) model, three main pores with sizes of 5.2, 7.8-8.5, and 10.5 Å were detected in Al-TCPP. In the DFT method, the pore is treated as a spherical shape [5]. According to our previous study [6], the size of the elliptical pore in Al-TCPP is 9.3 × 3.7 Å [elliptical] ≈ 5.8 Å[circle] and the rectangular pore is 9.3 × 6.1 Å≈7.8 Å[circle]. Based on this, the peak at 5.2 Å should be the contributed by the elliptical pore and the peaks at 7.8-8.5 Å are rectangular pores. The peak at 10.5 Å could be contributed by caused by the random aggregation of nanosheets [6].

Mott-Schottky plots (FigureS8)

The flat band potential (E_{fb}) of Al-TCPP is probed to be -1.36 V vs. Ag/AgCl (pH 5.5) according to its Motto-Schottky plots. To convert the obtained E_{fb} vs. Ag/AgCl to it vs. RHE (NHE at pH=0), the following equation is used: $E_{NHE} = E_{Ag/AgCl} + 0.059\ pH + E^0_{\ Ag/AgCl}$, where E_{RHE} is the converted potential vs. RHE, $E^0_{Ag/AgCl} = 0.1976$ at 25 °C, and $E_{Ag/AgCl}$ is the experimentally measured potential against Ag/AgCl reference. The flat band potential of Al-TCPP is calculated to be -0.84 V vs. NHE.

^{1}H NMR spectra of oxidized benzyl alcohol product (Figure S13)

For ^{1}H NMR spectra, the resonance at 10.00 ppm corresponds to the aldehyde group of benzaldehyde, and the resonance at 8.14 ppm corresponds to the carboxylic acid of benzoic acid, which could be used to distinguish them. According to Figure11b, there is only one resonance at 10 ppm and no resonance at 8.14 ppm is detected in all the samples, indicating only benzaldehyde is present in the organic phase after photocatalysis for 3 hours.

High-resolution XPS spectra (Figure S28)

The electron binding energy of porphyrin in the C1s spectrum of Al-TCPP shows a positive shift (+0.5 eV), comparing that in TCPP (Figure S28a). Similarly, a positive shift (+0.4 eV) of binding energy is observed in N1s spectra (Figure S28b). Generally, the presence of charge transfer between two components causes shifts of binding energy in their XPS spectra, wherein a positive shift indicates electron donation happens. Thereby, the obvious positive shift of binding energy in the C1s and N1s spectra implies the electrons transfer process from porphyrin to Al node in Al-TCPP.

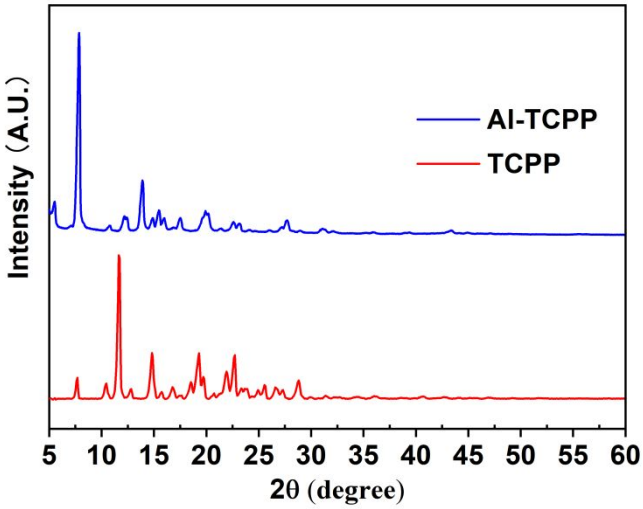

Figure S1. Laboratory XRD patterns of Al-TCPP and pristine TCPP powder

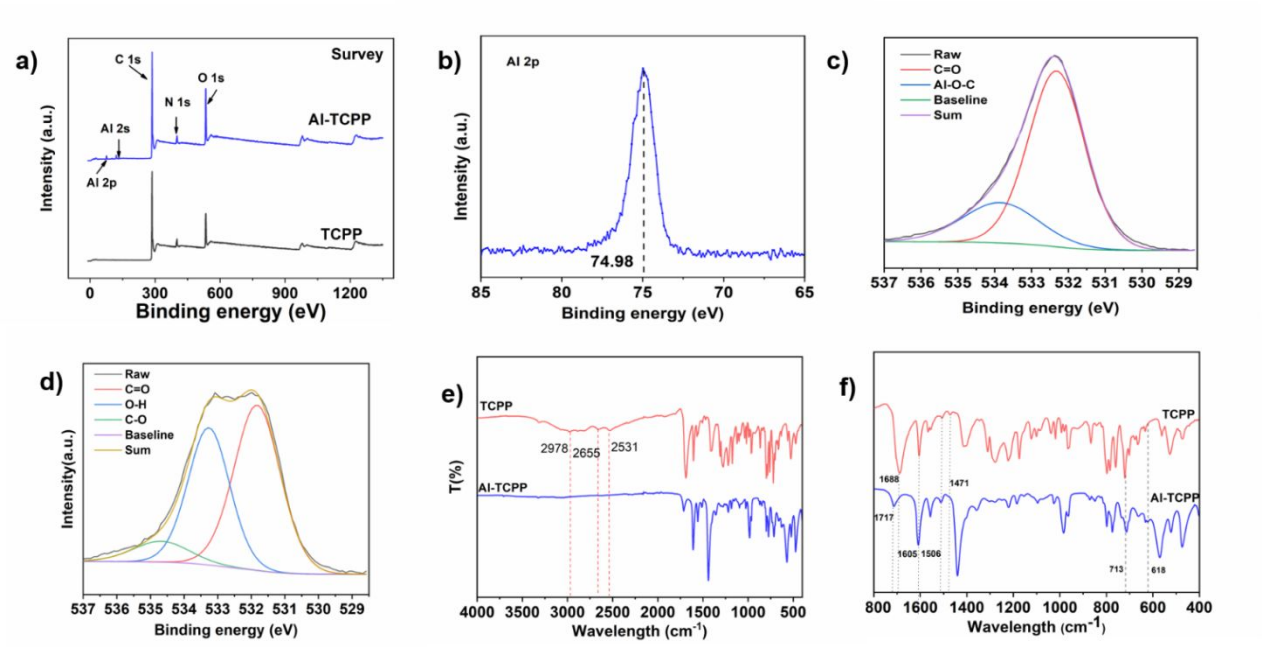

Figure S2. XPS survey spectra (a) of Al-TCPP and TCPP; high-resolution Al 2p (b) and O 1s (c) of Al-TCPP, O 1s (c) of TCPP, Fourier transform infrared (FTIR) spectra (e) of Al-TCPP and TCPP and enlarged area (800-400 cm^{-1}, f) FTIR spectra of Al-TCPP and TCPP.

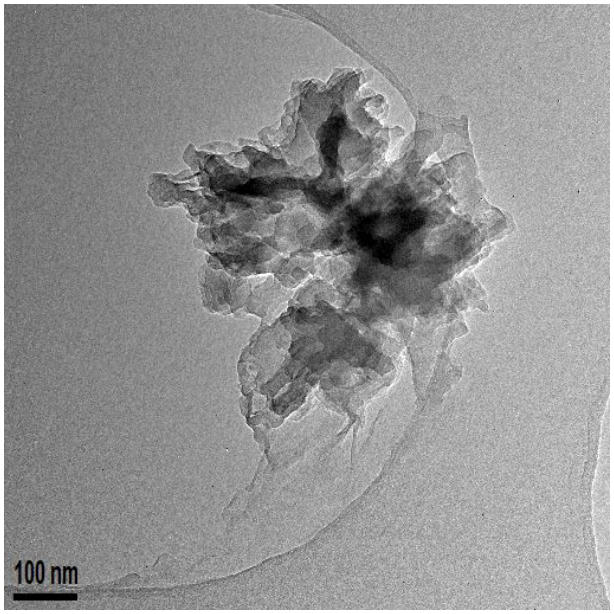

Figure S3. TEM image of pristine TCPP sample

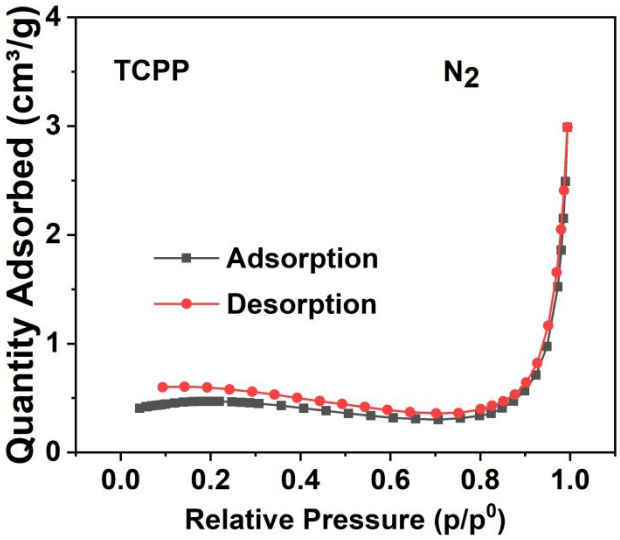

Figure S4. N_2 adsorption and desorption plots of TCPP powder at 77K. The surface area of TCPP is calculated to be 1.4045 m^2/g according to Langmuir Model

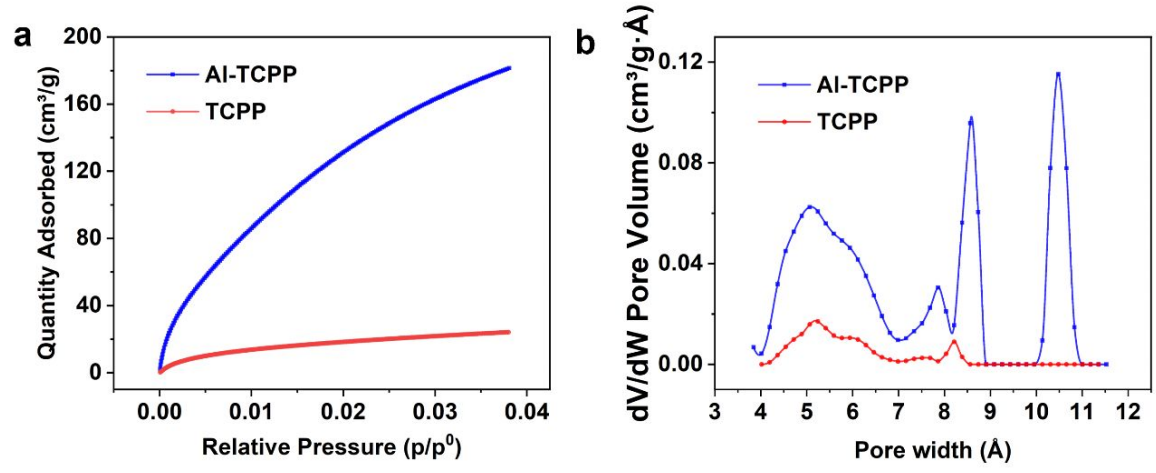

Figure S5 CO_2 adsorption of Al-TCPP and TCPP at 273K (c), and its corresponding pore size distribution obtained from the DFT model (b).

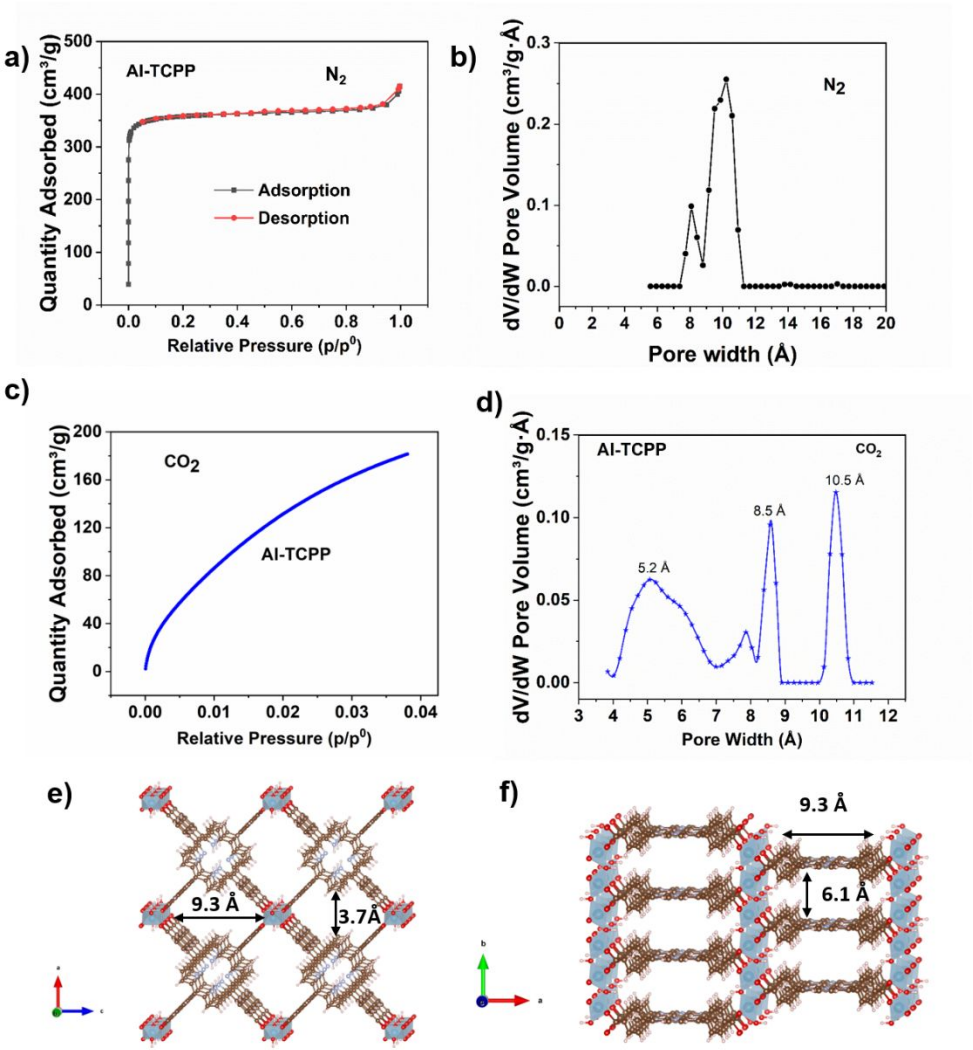

Figure S6 N_2 adsorption and desorption plots (a) and the corresponding pore size distribution of Al-TCPP (b); CO_2 adsorption of Al-TCPP at 273K (c), and its corresponding pore size distribution obtained from the DFT model (d); Elliptical pores (9.3×3.7 Å) viewed down [010] (e) and rectangular pores (9.3×6.1 Å) viewed down [001] direction (f).

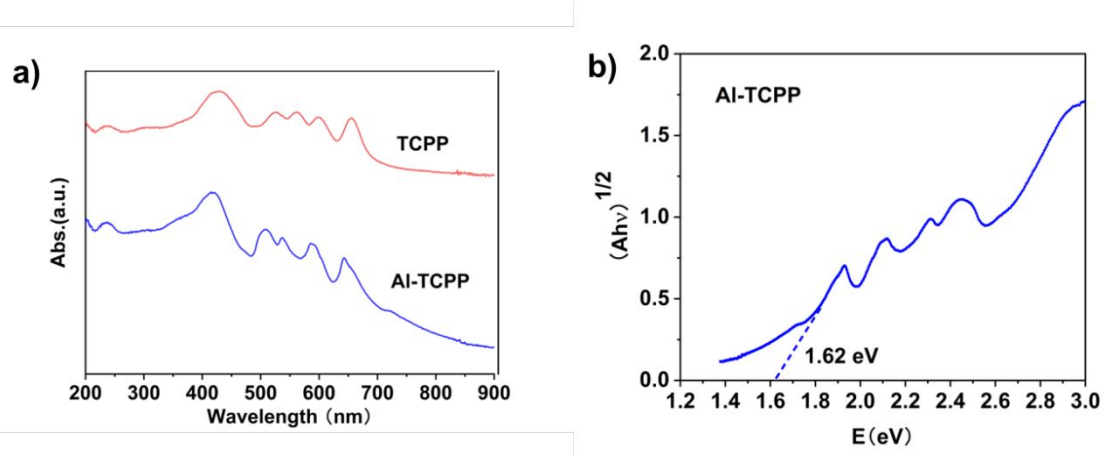

Figure S7. Solid UV-vis absorption spectra of Al-TCPP and TCPP powder (a); the Tauc plot of Al-TCPP (b). Note that to better display the sharp Soret band of the sample, we diluted our samples with BaSO4 at a mass ratio of 1:10.

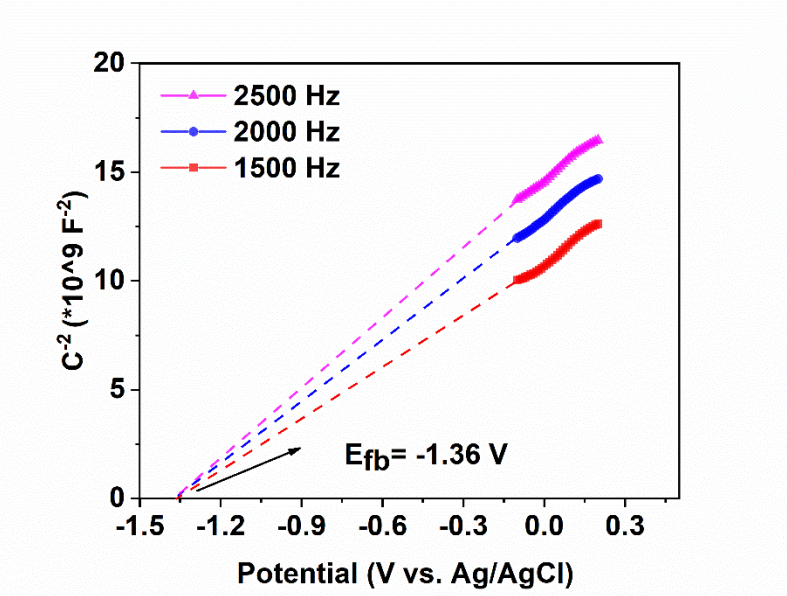

Figure S8 Mott-Schottky plots of Al-TCPP electrode tested with different frequencies.

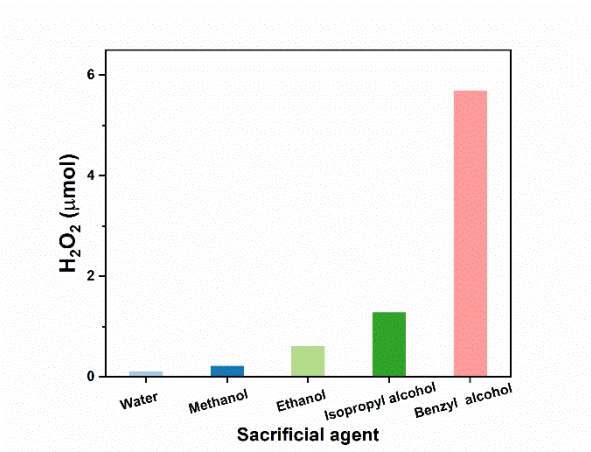

Figure S9 Photocatalytic H_2O_2 production by Al-TCPP with different hole sacrificial organic reagent. Reaction conditions: catalyst 7.5 mg; Water: 24 ml; organics: 6 ml; visible light irradiation for 20 minutes.

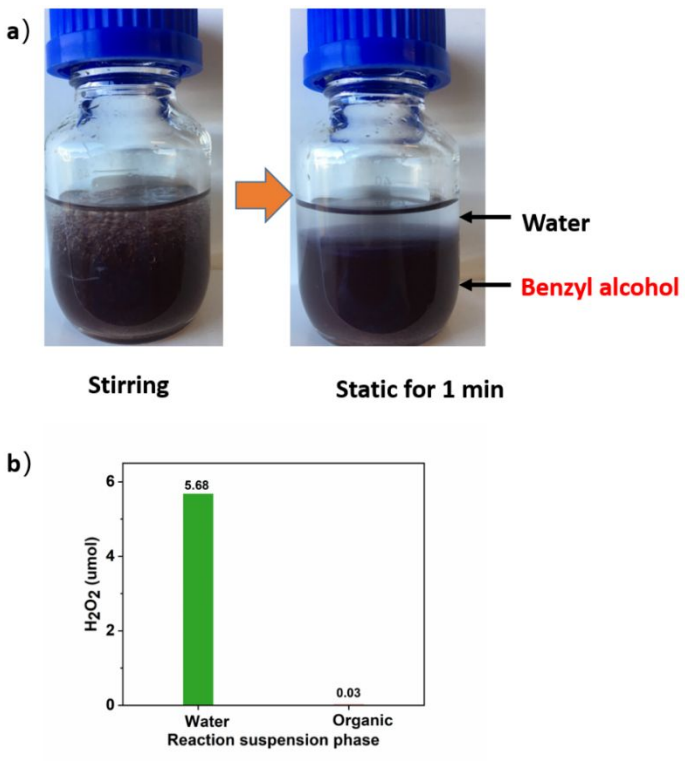

Figure S10. (a) Pictures of Al-TCPP-benzyl alcohol suspension mixed with water under stirring conditions (left) and after static treatment (right). After a short time (within 1min), the catalyst/benzyl alcohol suspension and water form two phases; (b) H_2O_2 amount in water and benzyl alcohol phase after photocatalysis reaction: Reaction conditions: catalyst 7.5 mg; Water: 24 ml; benzyl alcohol: 6 ml; visible light irradiation for 20 minutes.

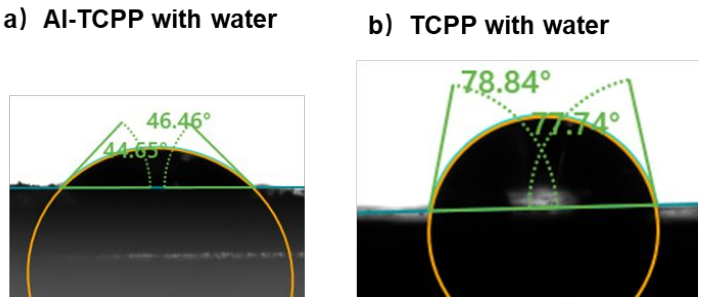

Figure S11. Contact angel of Al-TCPP(a) and TCPP (b) with water

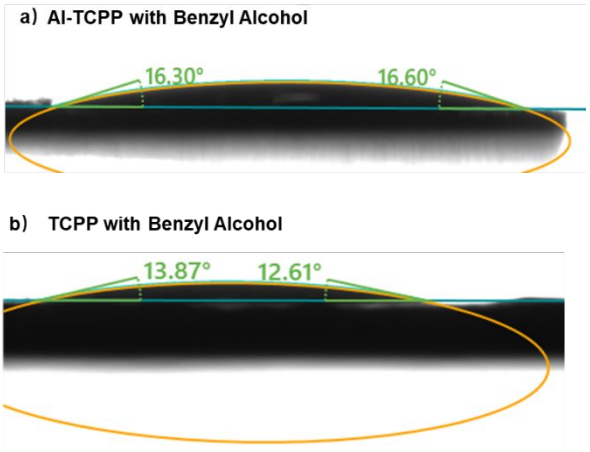

Figure S12. Contact angel of Al-TCPP(a) and TCPP (b) with benzyl alcohol.

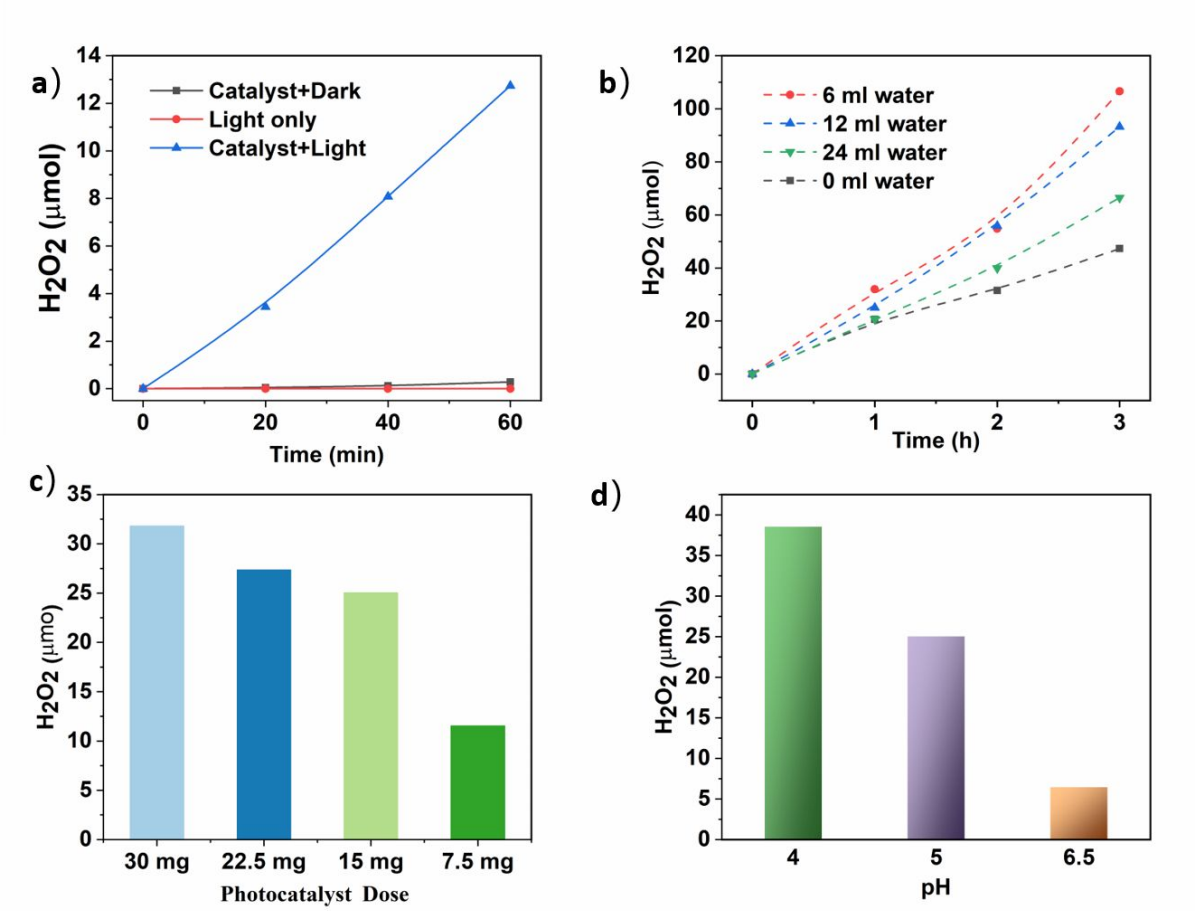

Figure S13. (a) Effect of different reaction conditions for H_2O_2 generation by Al-TCPP photocatalysis; (b) Effect of water content on H_2O_2 generation by Al-TCPP in the two-phase system Reaction conditions: 15 mg catalyst was dispersed in 24 ml benzyl alcohol, visible light irradiation for 3 hours. (c) Effect of catalyst dose on H_2O_2 generation by Al-TCPP in the two-phase system Reaction conditions: 12 ml water, 24 ml benzyl alcohol, visible light irradiation for 1our; (d) Effect of the pH of water on H_2O_2 generation by Al-TCPP in the two-phase system Reaction conditions: 12 ml water, 24 ml benzyl alcohol, 15 mg catalyst, visible light irradiation for 1 hour.

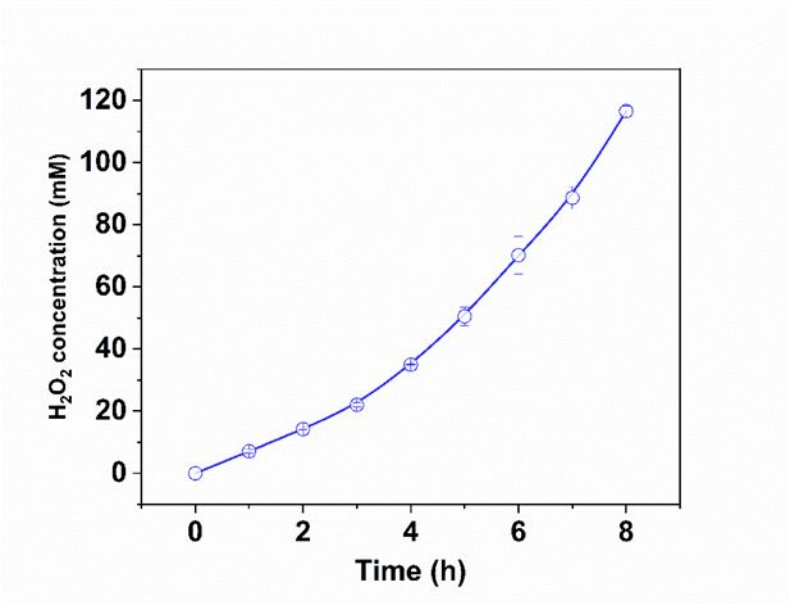

Figure S14 Concentration change of H_2O_2 aqueous solution with Al-TCPP under simulated solar light for 8 hours. Note: the volume of the water phase decreased from 12 ml to ~7.75 ml due to the evaporation in an open reaction system in 8 hours;

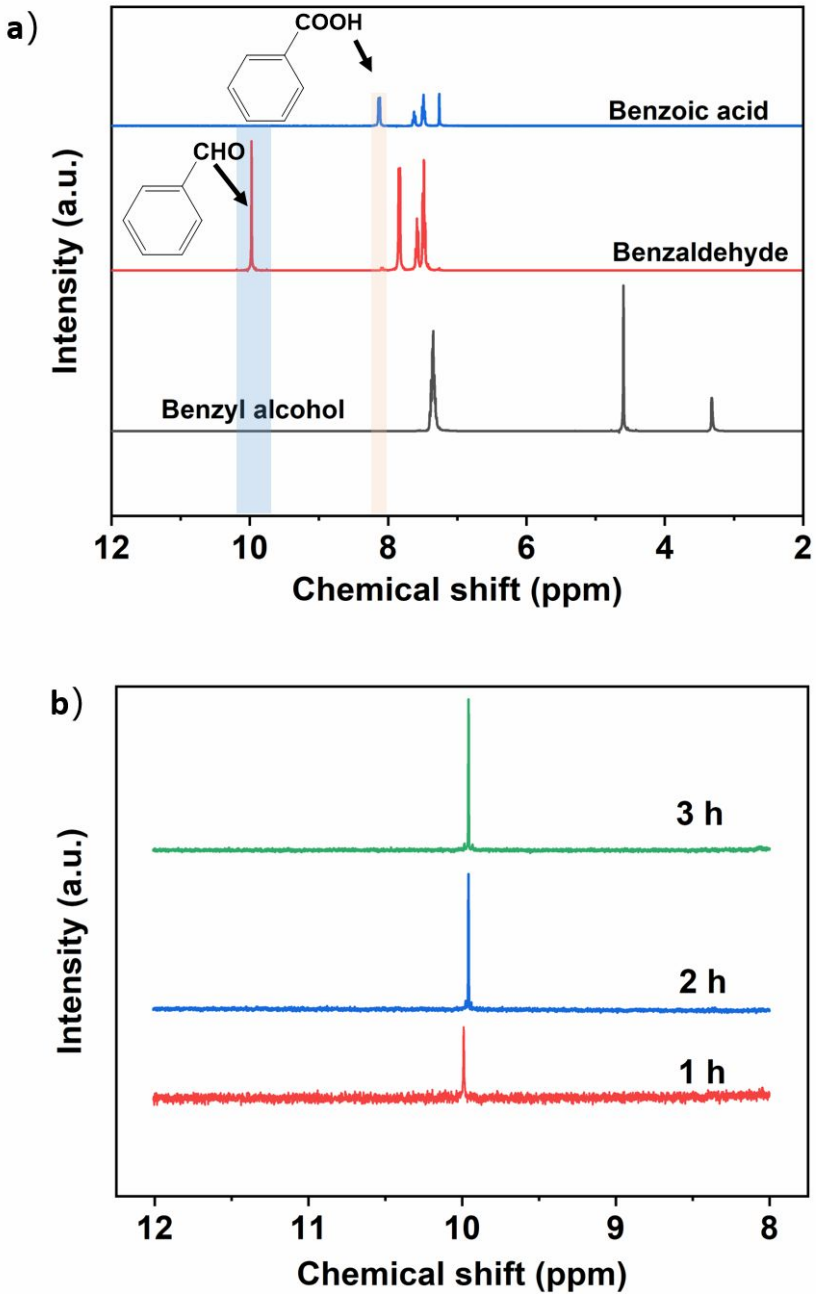

Figure S15. (a) ^{1}H NMR spectra of benzyl alcohol, benzaldehyde, and benzoic acid standards. (b) ^{1}H NMR spectra (12-8 ppm chemical shift range) of benzyl alcohol phase after treatment by Al-TCPP photocatalysis for 1h, 2h, and 3h under visible light.

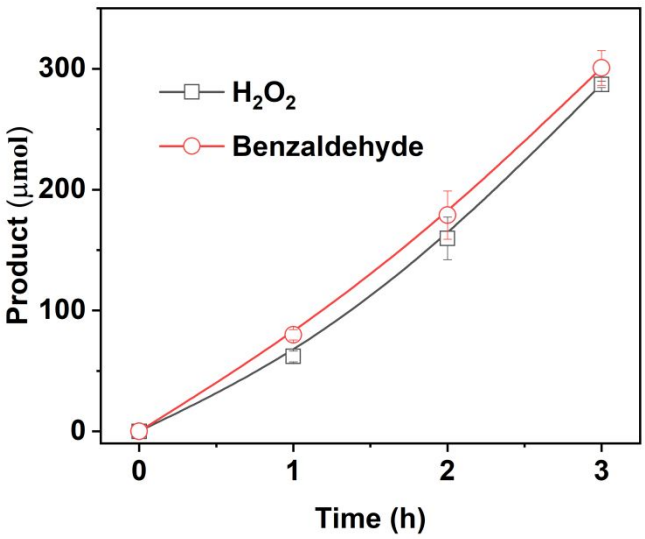

Figure S16 H_2O_2 and benzaldehyde generation by Al-TCPP simulated AM1.5 solar light irradiation (100 mW/cm^2); Reaction conditions: 12 ml water (pH 4.0), 24 ml benzyl alcohol, 15mg catalyst. After reaction for 3h, the mole ratio of H_2O_2 (287.06±2.63 μmol) to benzaldehyde (300.7±14.38) is close to 1:1.

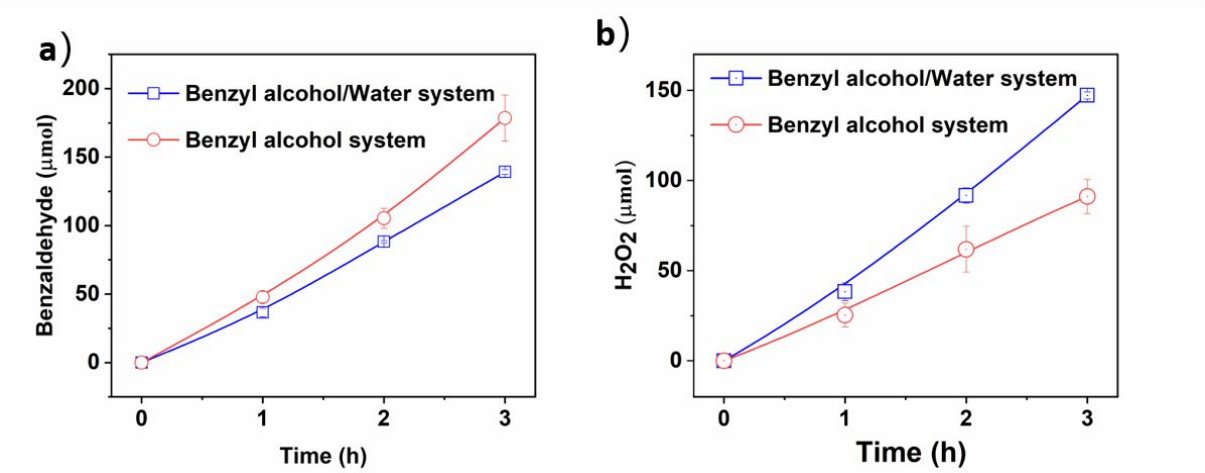

Figure S17. Benzaldehyde (a) and H_2O_2 (b) generation by Al-TCPP in benzyl alcohol/water two-phase system and benzyl alcohol system. Two-phase system: 12 ml water and 24ml benzyl alcohol; benzyl alcohol system: 24ml benzyl alcohol; 15 mg catalyst; visible light irradiation.

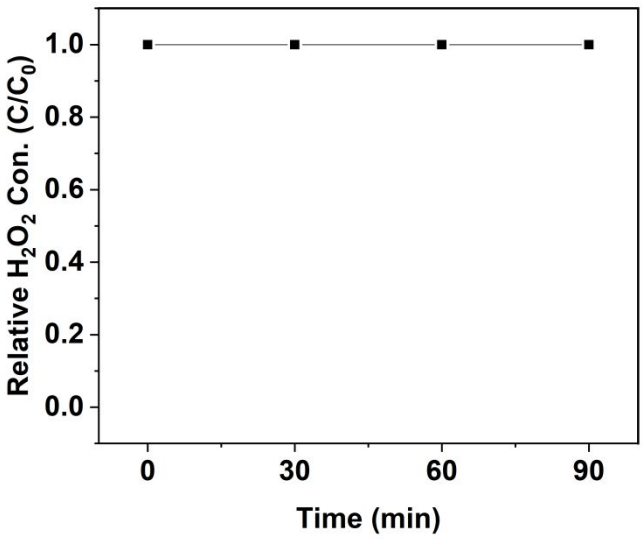

Figure S18 H_2O_2 decomposition by Al-TCPP suspension. Condition: 100 μmol H_2O_2, 15 mg Al-TCPP, 30 ml water, dark.

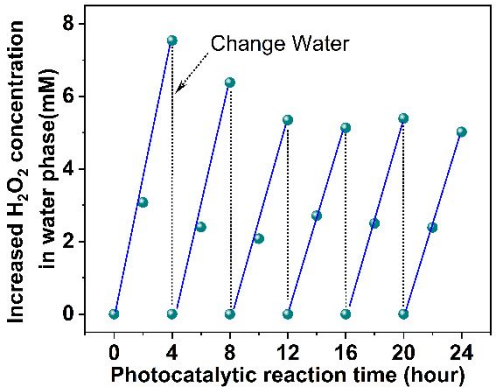

Figure S19. H_2O_2 production by Al-TCPP under 24-hour light irradiation. Condition:7.5 mg Al-TCPP photocatalyst, 12 ml water, 24ml benzyl alcohol, visible light irradiation. Please note that the organic phase with photocatalyst was separated by a separatory funnel and then 12ml fresh water was added to the reaction.

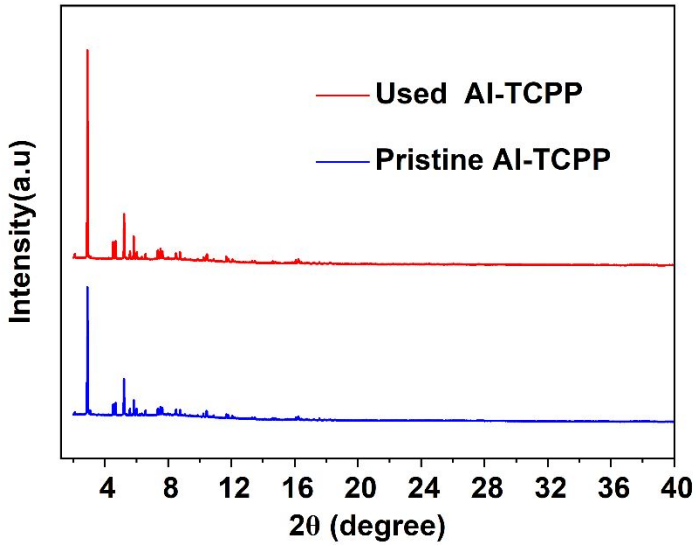

Figure S20 Synchrotron X-ray powder XRD patterns of pristine Al-TCPP and used Al-TCPP photocatalyst after the 3-cycle reaction. Wavelength λ=0.5903 Å

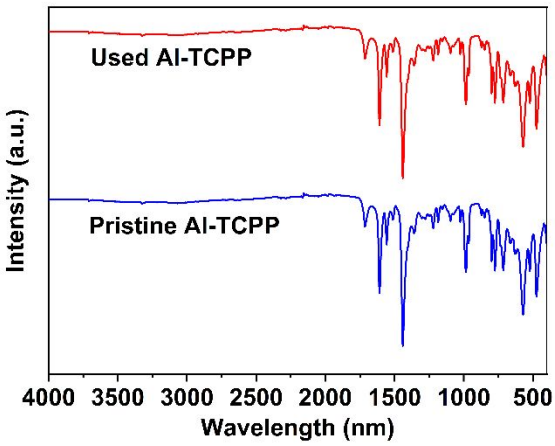

Figure S21. FTIR spectra of pristine and used Al-TCPP

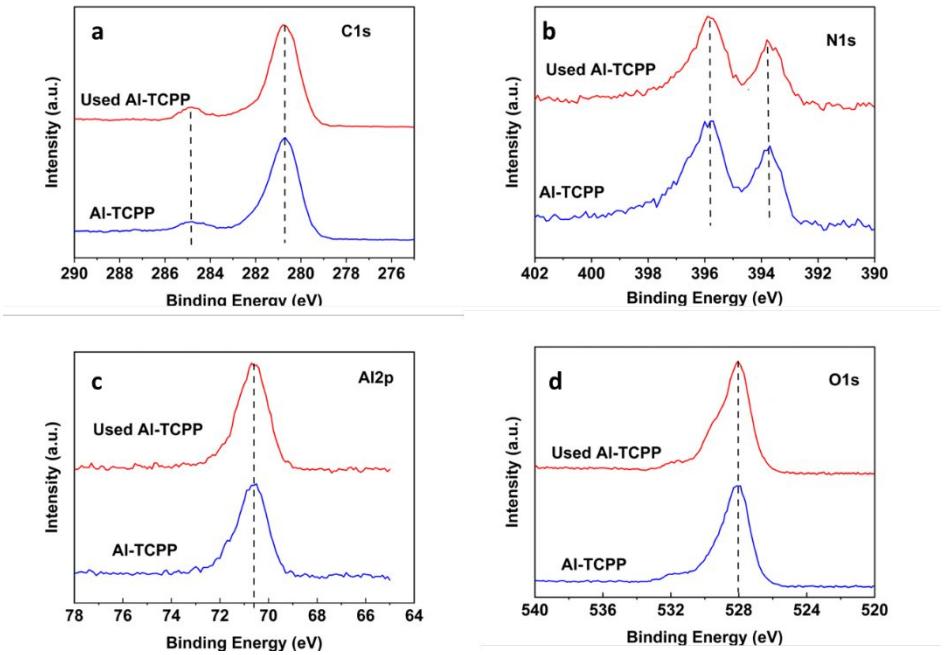

Figure S22. C1s (a), N1s (b), Al2p (c) and O1s (d) XPS spectra of pristine and used Al-TCPP after photocatalysis.

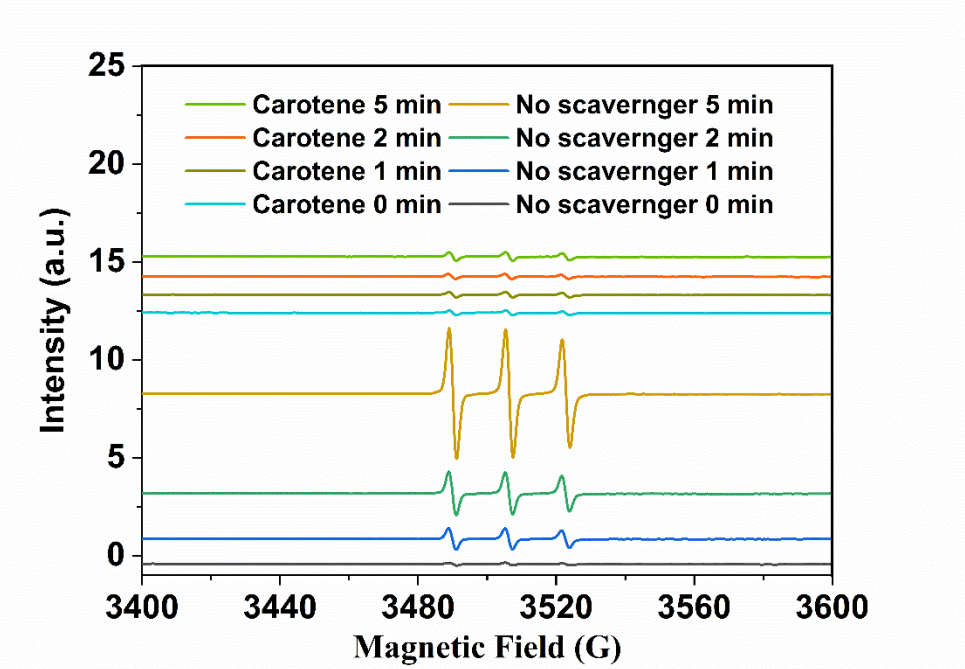

Figure S23 EPR spectra of TEMPO-$^1O_2$ by Al-TCPP benzyl alcohol-water photocatalysis system with 100 μmol carotene and without any scavenger. With carotene in the system, the signal of $^1O_2$ is almost decimated, indicating the scavenger role of carotene to $^1O_2$.

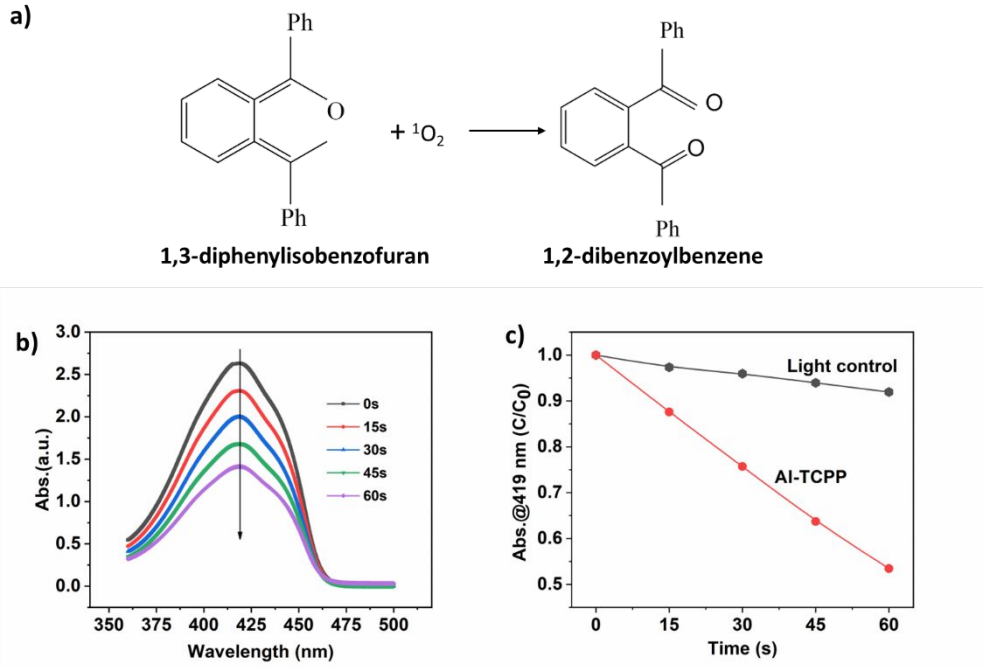

Figure S24 Scheme of singlet oxygen react with 1,3-diphenylisobenzofuran (a); The adsorption spectra of 1,3-diphenylisobenzofuran with Al-TCPP for different time (b); The change of adsorption at 419 nm of 1,3-diphenylisobenzofuran with Al-TCPP and without catalyst (light control) under visible light irradiation.

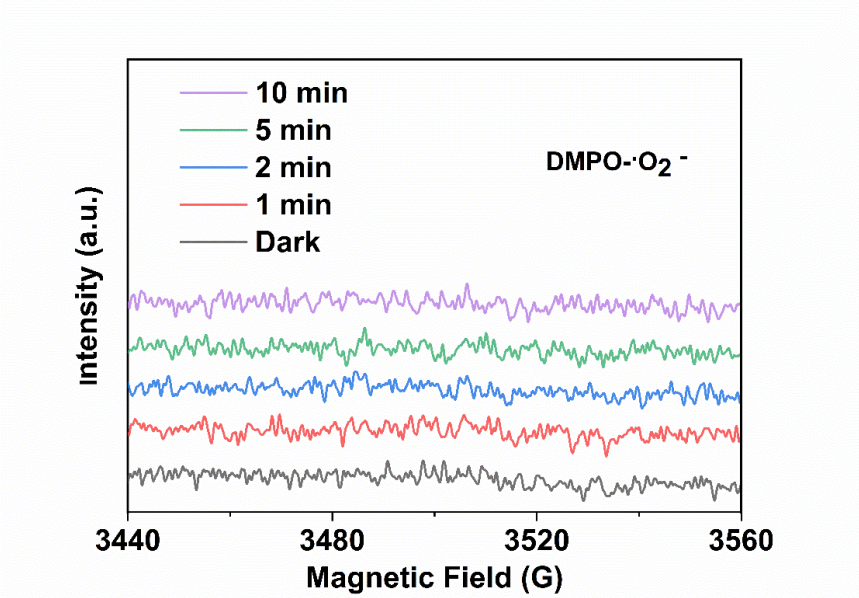

Figure S25 EPR spectra of DMPO-$\cdot O_2^-$ by Al-TCPP benzyl alcohol-water photocatalysis system with different irradiation time.

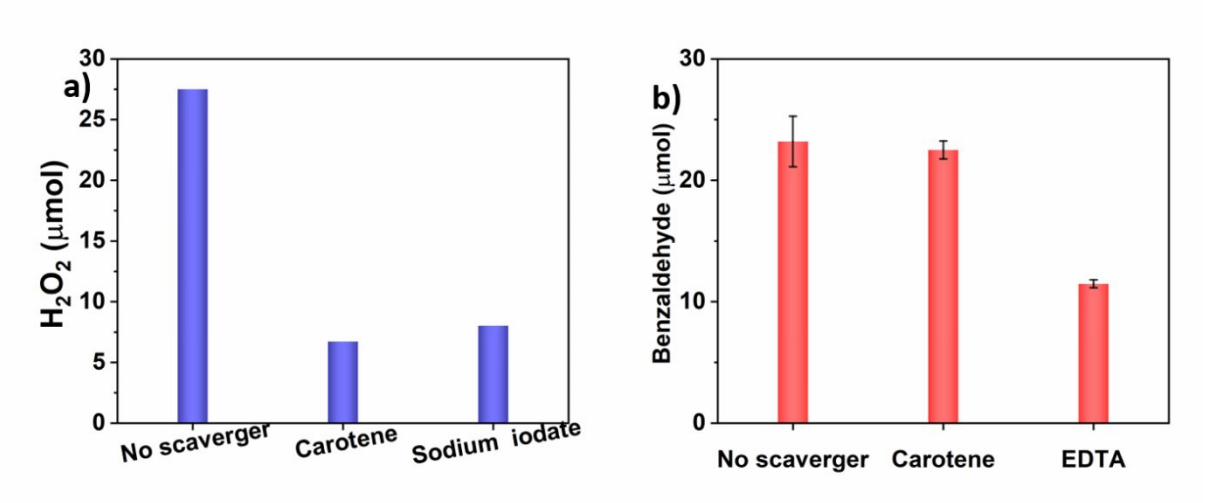

c)

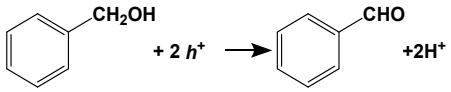

Figure S26. (a) Effect of carotene (single oxygen scavenger) and sodium iodate (electron scavenger) on the H_2O_2 production by Al-TCPP; (b) Effect of carotene (single oxygen scavenger) and EDTA (hole scavenger) on the benzaldehyde production by Al-TCPP; (c) Scheme for the photo-oxidation of benzyl alcohol by holes to benzaldehyde.

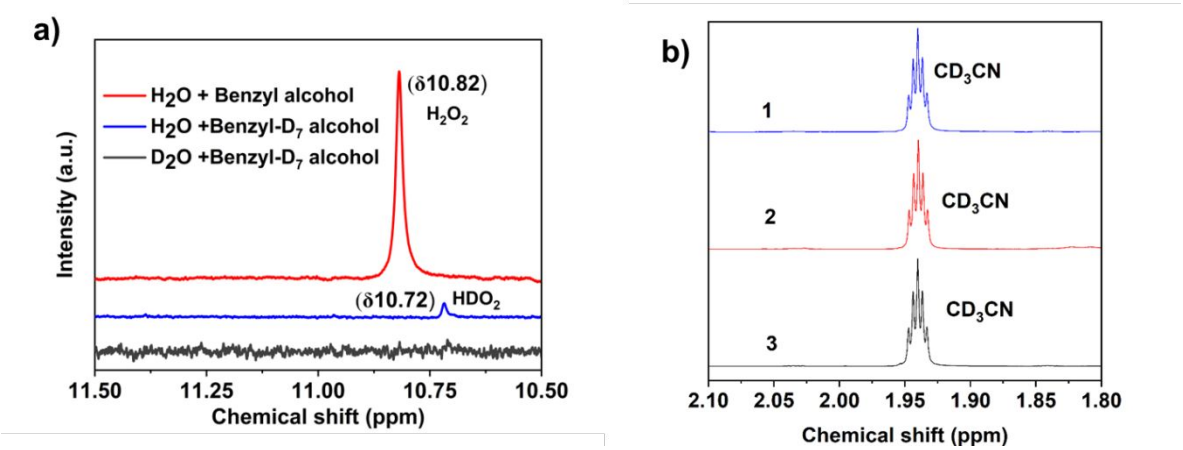

Figure S27. (a) ^{1}H NMR spectra of photocatalysis products in different proton sources. Red: H_2O (pH 4.0) and benzyl alcohol; Blue: H_2O (pH 4.0) and Benzyl-D_7 alcohol; Black: D_2O and Benzyl-D_7 alcohol. (b) ^{1}H NMR spectra of CD_3CN. Please note the chemical shift of CD_3CN is used as the internal reference. For all the three experiments, the chemical shift of CD_3CN is the same (1.93 ppm).

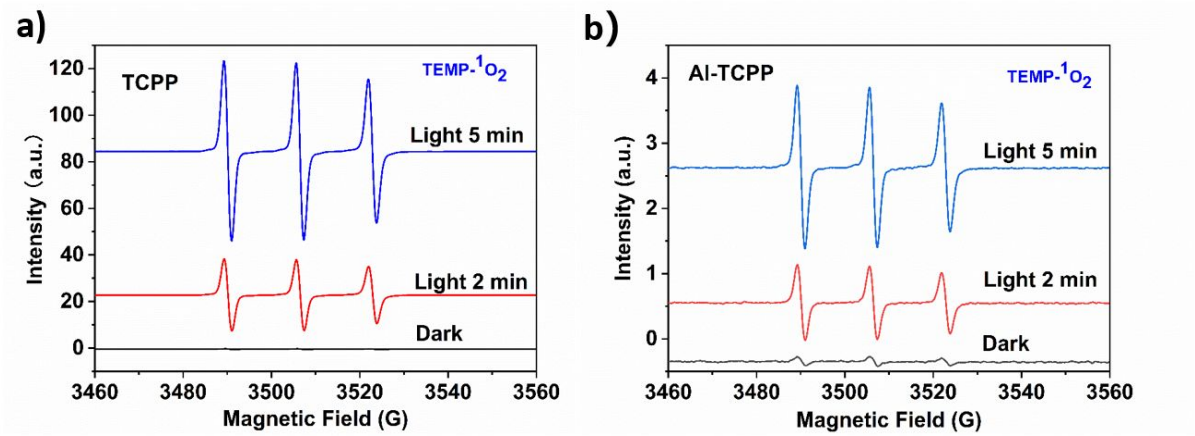

Figure S28. EPR spectra of TEMPO-$^1O_2$ by TCPP (a) and Al-TCPP in benzyl alcohol-water photocatalysis system. The signal by TCPP is around 20 times stronger than that by Al-TCPP after irradiation for 5 min.

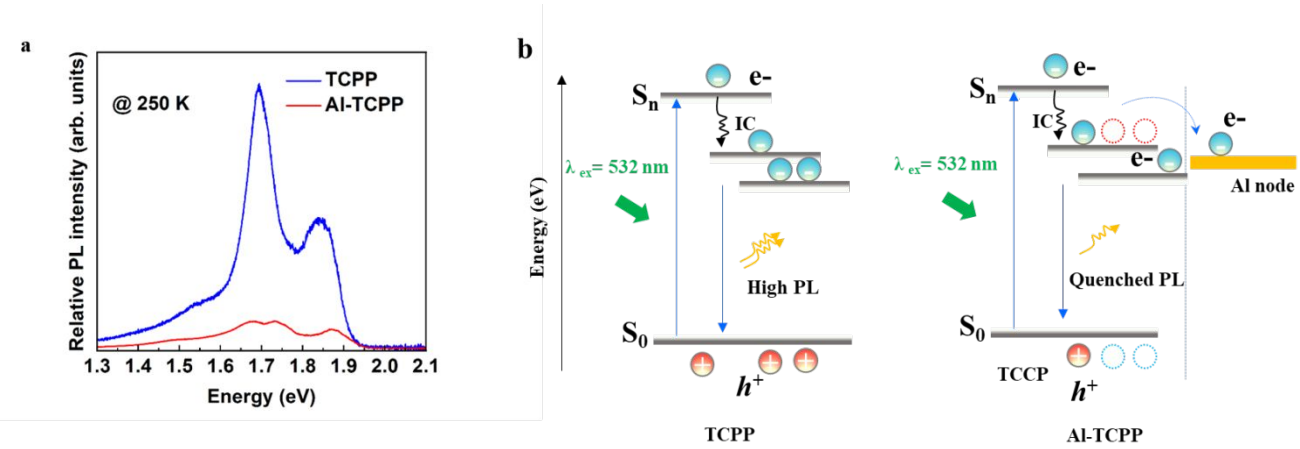

Figure S29 (a) PL spectra of TCCP and Al-TCCP on Si/SiO_2 substrate excited under 532-nm laser. (b) Proposed band illustration of the photoexcitation process in TCCP (left) and Al-TCCP (right). S_n is the electronic state of resonance when the MOFs are excited with the laser source. S_0 is the electronic ground state. In TCCP, a strong PL intensity is observed due to a total emission, with some interruption from shallow trap impurities (peak energy at 1.69 eV) after an internal conversion (IC) of molecules' relaxation prior to falling back to the vibration states in S_0. In comparison, there is an observed quenching of Al-TCCP PL which is due to only part of the carrier population falling back to S_0 and the remaining part rapidly crossing to the Al in the MOF.

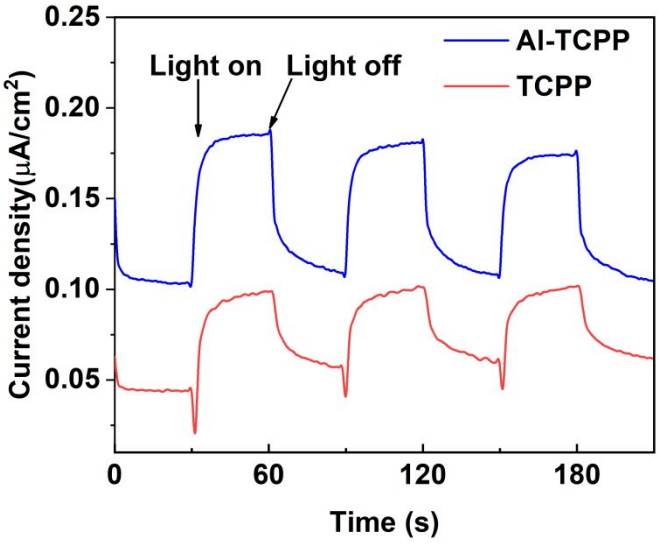

Figure S30. Photocurrent response by Al-TCPP and TCPP electrodes under visible light irradiation.

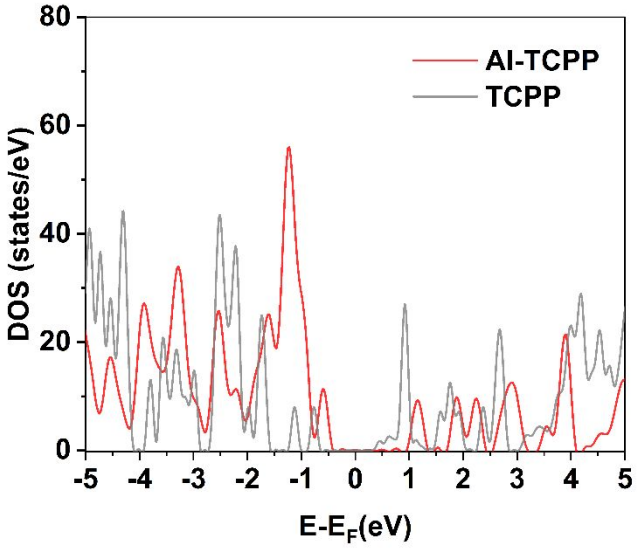

Figure S31 Density of states (DOS) analysis of Al-TCPP and TCPP.

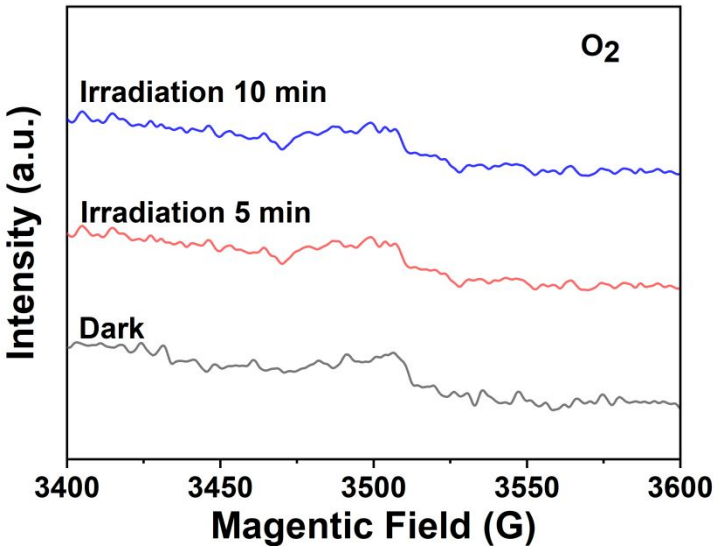

Figure S32. *In-situ* irradiated EPR signal of Al-TCPP benzyl alcohol suspension with O_2

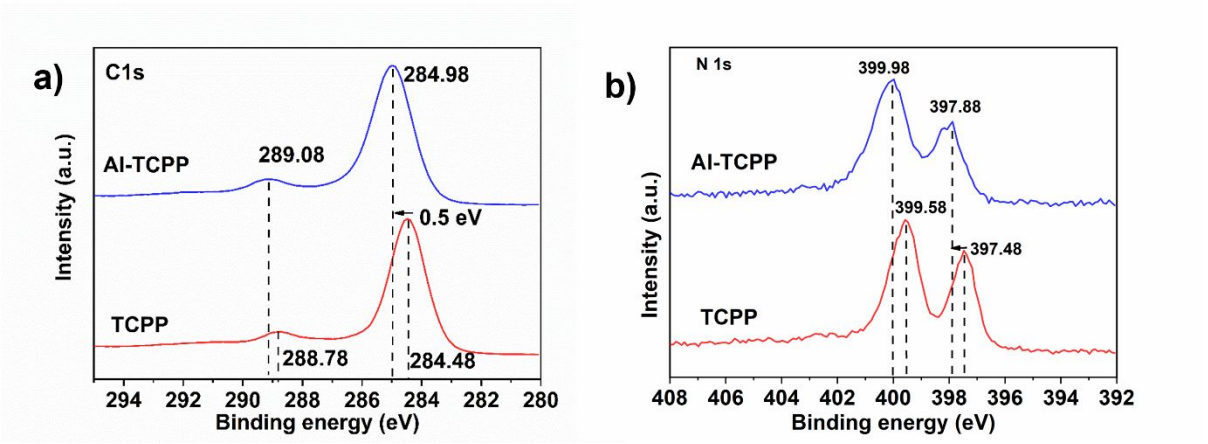

Figure S33. High-resolution C 1s (a) and N1s (b) spectra of Al-TCPP and TCPP**.**

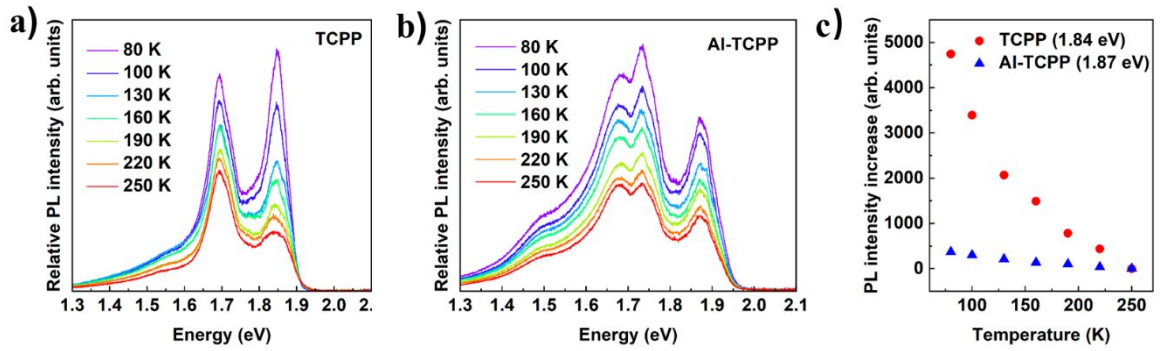

Figure S34 Temperature dependent PL measurements. Temperature-dependent relative PL spectra from (A)TCCP and (B) Al-TCCP showing the evolution of different PL peaks in the two materials. (C) . Summary of the evolution of high energy peak at 1.84 eV in TCCP and 1.87 eV in Al-TCCP which shows poor charge transfer in TCCP characterised by increased PL intensity at band-band emission.

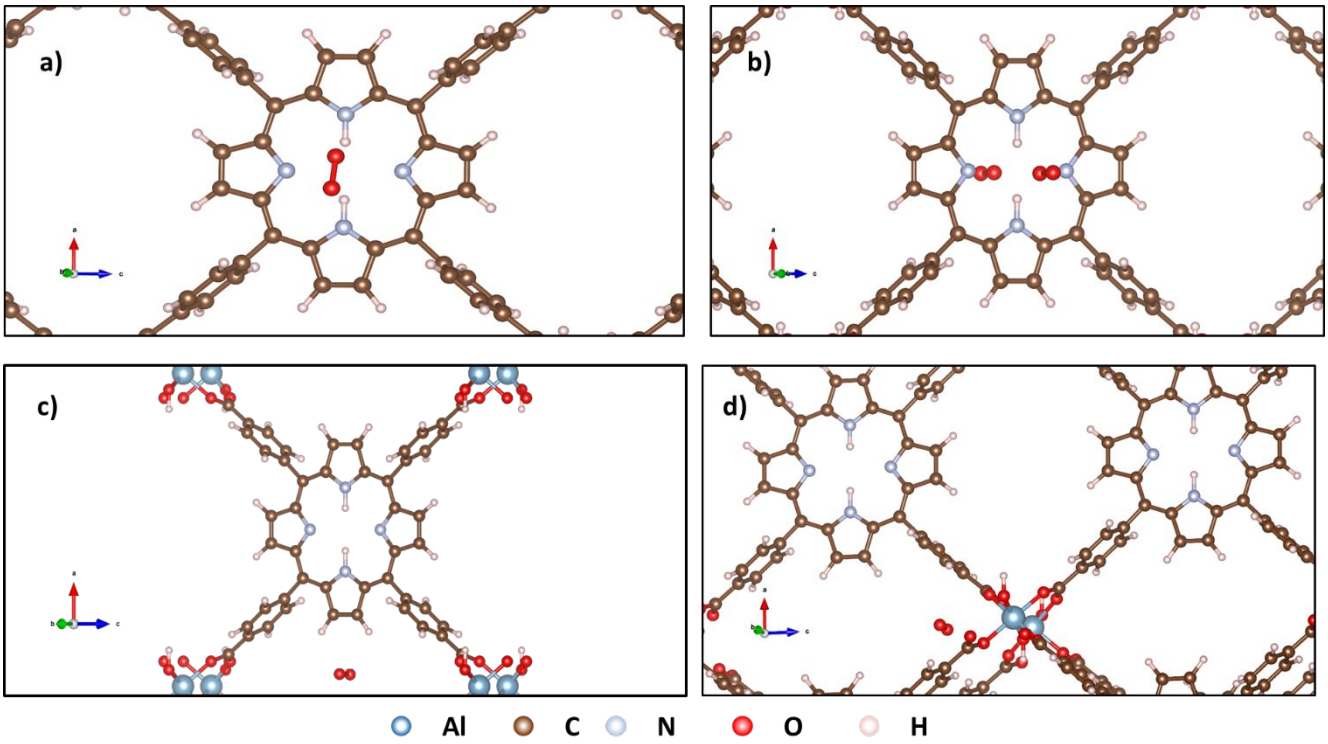

Figure S35 Optimized models for the adsorption of O_2 to Al-TCPP at different sites: (a) above the middle of porphyrin ring; (b) off centre above of porphyrin ring; (c) β-C of porphyrin channel; (d) surround the Al node.

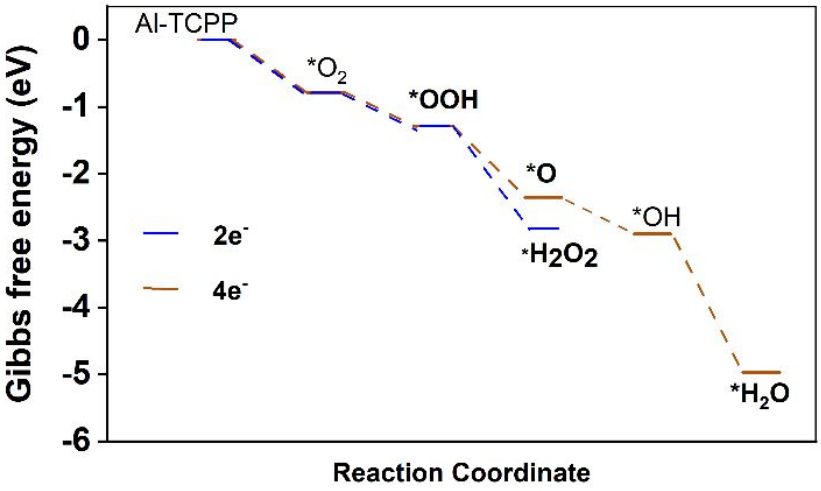

Figure S36 The energy profile of O_2 reduction to H_2O_2 ($2e^-$) and H_2O ($4e^-$) on the β-C of porphyrin channel with singlet state oxygen.

Table S1. Crystal parameters of pristine and used Al-TCPP catalysts through structure refinement.

	Al-TCPP	Used Al-TCPP
Spacegroup	*Cmmm*	*Cmmm*
Cell Volume (Å^3)	3559.79 (12)	3556.75 (12)
Rwp % - Rietveld	3.41%	3.65%
Crystallite size LVol-IB (nm)	166.3(2)	206.4(2)
Lattice parameters		
a(Å)	31.8753(6)	31.8539(7)
b (Å)	6.61289(7)	6.60395(9)
c (Å)	16.8880(4)	16.9081(4)

Table S2. Surface area analysis of Al-TCPP and TCPP by N_2 adsorption at 77K and CO_2 adsorption at 273K

	N_2	**CO_2**
Kinetic diameter of gas molecule	3.46 Å	3.30 Å
Surface area- Al-TCPP	1447 m^2/g	1287.75 $m^2\ g^{-1}$
Surface area-TCPP	1.4045 m^2/g	165.38 $m^2\ g^{-1}$

Table S3. Comparison of photocatalytic H_2O_2 production by reported catalysts

Catalyst	**Dose (mg)**	**Reaction system ***	Sacrificial reagent	**Light**	**H_2O_2 yield rate (μmol h^{-1} $g^{-1}_{catalyst}$)**	**AQY**	**Ref.**
TiO_2	50	BA: 350 mM H_2O: 5 mL	benzyl alcohol	Vis. (λ>420 nm)	35.8	N/A	[7]
MIL-125-R7	5	BA: 5 mL H_2O 2 mL	benzyl alcohol	Vis. (λ>420 nm)	1600	N/A	[8]
OPA-$Zr_{92.5}$ $Ti_{7.5}$-MOF	5	BA: 5 mL H_2O 2 mL	benzyl alcohol	Vis. (λ>420 nm)	3660	N/A	[9]
OPA-Fe-Zr-MOF	5	BA: 5 mL H_2O 2 mL	benzyl alcohol	Vis. (λ>420 nm)	5320	N/A	[10]
TAPD-$(Me)_2$-COF	20	BA: 4.5 mL H_2O:0.5 mL	benzyl alcohol	Vis. (λ>420 nm)	167.5	N/A	[11]
ZrS_3 nanobelt	50	BA: 1 mmol H_2O: 30 mL	benzyl alcohol	Solar (AM 1.5G)	1792	11.4% at 400nm 10.8% at 500nm	[12]
Amphiphilic g-C_3N_4	10	BA: 5 mL H_2O: 25 mL	benzyl alcohol	Vis. (λ>420 nm)	2880	_	[13]
sonoCOF-F2	50	BA: 27 mL H_2O: 3 mL	benzyl alcohol	Vis. (λ>420 nm)	414.6	_	[14]
PMCR-1	20	BA: 2 mL H_2O: 20 mL	benzyl alcohol	400–700 nm	5500	14% at 420 nm	[15]
EBA-COF	20	BA: 2 mL H_2O: 20 mL	benzyl alcohol	420nm LED	2550	4.4% at 420 nm	[16]
P-TAME	20	phenylcarbinol: 2 mL H_2O: 18ml	phenylcarbinol	λ = 420 nm	9500	N/A	[17]
COFs@Pd	10	Ethanol: 2 ml H_2O: 18ml	Ethanol	Solar (AM 1.5G)	2143	6.5% (420nm)	[18]
TTH–CTP	10	BA: 2 mL H_2O: 18ml	benzyl alcohol	Xe lamp	**23700**	11.3% (450 nm) 0% at 600 nm 0% at 700 nm	[19]
TaptBtt	15	H_2O 10 mL	H_2O	300 W Xe lamp λ > 420 nm	1407	4.6 % at 450 nm	[20]
Al-TCPP	15	BA: 24 mL H_2O 12 mL	benzyl alcohol	Vis. (λ>400 nm)	3391.3	12.11% at 420 nm, 7.49% at 500 nm, 5.33% at 600 nm, 3.48% at 700 nm	This work
Al-TCPP	15	BA: 24 mL H_2O: 12 mL	benzyl alcohol	Solar (AM 1.5G)	6378		This work

Table S4. The adsorption energy of O_2 to the sites of Al-TCPP

Adsorption site	**Model**	**Triplet Adsorption Energy (eV)**	**Singlet Adsorption Energy (eV)**
Above middle of porphyrin ring	Figure S29a	0.03	-0.55
Off Centre above of porphyrin ring	Figure S29b	0.06	-0.48
β-C of porphyrin ring	Figure S29c	-0.085	-0.79
Surrounding the Al node	Figure S29d	0.076	-0.42

References

(1) Rotole, J.; Sherwood, P. Boehmite (AlOOH-gamma) by XPS. *Surf Sci Spectra* **1998**, *5* (1), 53-59.
(2) Sun, B.; Ji, Z.; Liao, Y.-P.; Wang, M.; Wang, X.; Dong, J.; Chang, C. H.; Li, R.; Zhang, H.; Nel, A. E. Engineering an effective immune adjuvant by designed control of shape and crystallinity of aluminum oxyhydroxide nanoparticles. *ACS nano* **2013**, *7* (12), 10834-10849.
(3) Fateeva, A.; Chater, P. A.; Ireland, C. P.; Tahir, A. A.; Khimyak, Y. Z.; Wiper, P. V.; Darwent, J. R.; Rosseinsky, M. J. A water-stable porphyrin-based metal–organic framework active for visible-light photocatalysis. *Angewandte Chemie International Edition* **2012**, *51* (30), 7440-7444.
(4) Jagiello, J.; Thommes, M. Comparison of DFT characterization methods based on N2, Ar, CO2, and H2 adsorption applied to carbons with various pore size distributions. *Carbon* **2004**, *42* (7), 1227-1232.
(5) Landers, J.; Gor, G. Y.; Neimark, A. V. Density functional theory methods for characterization of porous materials. *Colloids and Surfaces A: Physicochemical and Engineering Aspects* **2013**, *437*, 3-32.
(6) Jian, M.; Qiu, R.; Xia, Y.; Lu, J.; Chen, Y.; Gu, Q.; Liu, R.; Hu, C.; Qu, J.; Wang, H. Ultrathin water-stable metal-organic framework membranes for ion separation. *Science advances* **2020**, *6* (23), eaay3998.
(7) Shiraishi, Y.; Kanazawa, S.; Tsukamoto, D.; Shiro, A.; Sugano, Y.; Hirai, T. Selective hydrogen peroxide formation by titanium dioxide photocatalysis with benzylic alcohols and molecular oxygen in water. *ACS Catalysis* **2013**, *3* (10), 2222-2227.
(8) Isaka, Y.; Kawase, Y.; Kuwahara, Y.; Mori, K.; Yamashita, H. Two-phase system utilizing hydrophobic metal–organic frameworks (MOFs) for photocatalytic synthesis of hydrogen peroxide. *Angewandte Chemie* **2019**, *131* (16), 5456-5460.
(9) Chen, X.; Kuwahara, Y.; Mori, K.; Louis, C.; Yamashita, H. A hydrophobic titanium doped zirconium-based metal organic framework for photocatalytic hydrogen peroxide production in a two-phase system. *Journal of Materials Chemistry A* **2020**, *8* (4), 1904-1910.
(10) Chen, X.; Kuwahara, Y.; Mori, K.; Louis, C.; Yamashita, H. Heterometallic and Hydrophobic Metal–Organic Frameworks as Durable Photocatalysts for Boosting Hydrogen Peroxide Production in a Two-Phase System. *ACS Applied Energy Materials* **2021**, *4* (5), 4823-4830.
(11) Krishnaraj, C.; Sekhar Jena, H.; Bourda, L.; Laemont, A.; Pachfule, P.; Roeser, J. r. m.; Chandran, C. V.; Borgmans, S.; Rogge, S. M.; Leus, K. Strongly reducing (diarylamino) benzene-based covalent organic framework for metal-free visible light photocatalytic H2O2 generation. *Journal of the American Chemical Society* **2020**, *142* (47), 20107-20116.
(12) Tian, Z.; Han, C.; Zhao, Y.; Dai, W.; Lian, X.; Wang, Y.; Zheng, Y.; Shi, Y.; Pan, X.; Huang, Z. Efficient photocatalytic hydrogen peroxide generation coupled with selective benzylamine oxidation over defective ZrS3 nanobelts. *Nature communications* **2021**, *12* (1), 1-10.
(13) Zhang, H.; Liu, M.; Zhang, X.; Yuan, B.; Wu, P.; Liu, C.; Jiang, W. On-site H2O2 production with amphiphilic g-C3N4 as photocatalyst in a combined photocatalysis–extraction–separation process. *Chemical Engineering Journal* **2022**, *438*, 135664.
(14) Zhao, W.; Yan, P.; Li, B.; Bahri, M.; Liu, L.; Zhou, X.; Clowes, R.; Browning, N. D.; Wu, Y.; Ward, J. W. Accelerated Synthesis and Discovery of Covalent Organic Framework Photocatalysts for Hydrogen Peroxide Production. *Journal of the American Chemical Society* **2022**.
(15) Das, P.; Roeser, J.; Thomas, A. Solar Light Driven H2O2 Production and Selective Oxidations using a Covalent Organic Framework Photocatalyst prepared by a Multicomponent Reaction. *Angewandte Chemie International Edition* **2023**, e202304349.
(16) Zhai, L.; Xie, Z.; Cui, C.-X.; Yang, X.; Xu, Q.; Ke, X.; Liu, M.; Qu, L.-B.; Chen, X.; Mi, L. Constructing synergistic triazine and acetylene cores in fully conjugated covalent organic frameworks for cascade photocatalytic H2O2 production. *Chem. Mat.* **2022**, *34* (11), 5232-5240.
(17) Luo, Z.; Chen, X.; Hu, Y.; Chen, X.; Lin, W.; Wu, X.; Wang, X. Side-Chain Molecular Engineering of Triazole-Based Donor-Acceptor Polymeric Photocatalysts with Strong Electron Push-Pull Interactions. *Angewandte Chemie* **2023**, *135* (30), e202304875.
(18) Liu, Y.; Li, L.; Tan, H.; Ye, N.; Gu, Y.; Zhao, S.; Zhang, S.; Luo, M.; Guo, S. Fluorination of covalent organic framework reinforcing the confinement of Pd nanoclusters enhances hydrogen peroxide photosynthesis. *Journal of the American Chemical Society* **2023**, *145* (36), 19877-19884.

(19) Wang, S.; Xie, Z.; Zhu, D.; Fu, S.; Wu, Y.; Yu, H.; Lu, C.; Zhou, P.; Bonn, M.; Wang, H. I. Efficient photocatalytic production of hydrogen peroxide using dispersible and photoactive porous polymers. *Nature Communications* **2023**, *14* (1), 6891.
(20) Qin, C.; Wu, X.; Tang, L.; Chen, X.; Li, M.; Mou, Y.; Su, B.; Wang, S.; Feng, C.; Liu, J. Dual donor-acceptor covalent organic frameworks for hydrogen peroxide photosynthesis. *Nature Communications* **2023**, *14* (1), 5238.